

The local luminosity function of star-forming galaxies derived from the *Planck* Early Release Compact Source Catalogue

M. Negrello^{1*}, M. Clemens¹, J. Gonzalez-Nuevo², G. De Zotti^{1,3}, L. Bonavera², G. Cosco⁴, G. Guarese⁴, L. Boaretto⁴, S. Serjeant⁵, L. Toffolatti⁶, A. Lapi^{3,7}, M. Bethermin⁸, G. Castex⁹, D. L. Clements¹⁰, J. Delabrouille⁹, H. Dole^{11,12}, A. Franceschini¹³, N. Mandolesi^{14,15}, L. Marchetti¹³, B. Partridge¹⁶, A. Sajina¹⁷

¹INAF, Osservatorio Astronomico di Padova, Vicolo Osservatorio 5, I-35122 Padova, Italy

²Inst. de Física de Cantabria (CSIC-UC), Avda. los Castros s/n, 39005 Santander, Spain

³SISSA, Via Bonomea 265, I-34136 Trieste, Italy

⁴Gruppo Astrofili Polesani, Osservatorio Astronomico Vanni Bazzan di Sant'Apollinare, I-45100 Rovigo, Italy

⁵Department of Physical Sciences, The Open University, Milton Keynes MK7 6AA, United Kingdom

⁶Departamento de Física, Universidad de Oviedo, Avda. Calvo Sotelo s/n, 33007 Oviedo, Spain

⁷Dipartimento di Fisica, Università 'Tor Vergata', Via Ricerca Scientifica 1, 00133 Roma, Italy

⁸Laboratoire AIM, IRFU/Service d'Astrophysique - CEA/DSM - CNRS - Université Paris Diderot, Bât. 709, CEA-Saclay, F-91191 Gif-sur-Yvette Cedex, France

⁹APC, 10, rue Alice Domon et Léonie Duquet, 75205 Paris Cedex 13, France

¹⁰Astrophysics Group, Imperial College, Blackett Laboratory, Prince Consort Road, London SW7 2AZ, UK

¹¹Institut d'Astrophysique Spatiale, CNRS (UMR 8617) Université Paris-Sud 11, Bâtiment 121, Orsay, France

¹²Institut Universitaire de France, 103, bd Saint-Michel, 75005, Paris, France

¹³Dipartimento di Fisica e Astronomia, Università di Padova, Vicolo dell'Osservatorio 3, I-35122 Padova, Italy

¹⁴INAF/IASF Bologna, Via Gobetti 101, Bologna, Italy

¹⁵Agenzia Spaziale Italiana, Viale Liegi 26, Roma, Italy

¹⁶Haverford College, Astronomy Department, 370 Lancaster Avenue, Haverford, Pennsylvania, USA

¹⁷Department of Physics and Astronomy, Tufts University, Medford, MA 02155, U.S.A.

Released 2012 Xxxxx XX

ABSTRACT

The *Planck* Early Release Compact Source Catalog (ERCSC) has offered the first opportunity to accurately determine the luminosity function of dusty galaxies in the very local Universe (i.e. distances $\lesssim 100$ Mpc), at several (sub-)millimetre wavelengths, using blindly selected samples of low redshift sources, unaffected by cosmological evolution. This project, however, requires careful consideration of a variety of issues including the choice of the appropriate flux density measurement, the separation of dusty galaxies from radio sources and from Galactic sources, the correction for the *CO* emission, the effect of density inhomogeneities, and more. We present estimates of the local luminosity functions at 857 GHz (350 μ m), 545 GHz (550 μ m) and 353 GHz (850 μ m) extending across the characteristic luminosity L_* , and a preliminary estimate over a limited luminosity range at 217 GHz (1382 μ m). At 850 μ m and for luminosities $L \gtrsim L_*$ our results agree with previous estimates, derived from the SCUBA Local Universe Galaxy Survey (SLUGS), but are higher than the latter at $L \lesssim L_*$. We also find good agreement with estimates at 350 and 500 μ m based on preliminary *Herschel* survey data.

Key words: galaxies: luminosity function – galaxies: photometry – galaxies: starburst – submillimetre: galaxies

1 INTRODUCTION

Our knowledge of the (sub-)millimetre luminosity function of galaxies has substantially improved in the last few years.

* mattia.negrello@oapd.inaf.it.

Before the launch of the *Herschel* Space Observatory (Pilbratt et al. 2010), no blind sub-mm surveys of sufficient area were available, and estimates of the local luminosity functions had to rely on follow-up of samples selected at other wavelengths. The most notable example is the local 850 μm luminosity function derived from the SCUBA Local Universe Galaxy Survey (SLUGS; Dunne et al. 2000) that provided SCUBA photometry of 104 galaxies drawn from the IRAS Bright Galaxy Survey (Soifer et al. 1989). Better constraints, particularly on the faint end of the 850 μm luminosity function as well as estimates of the luminosity function at many wavelengths in the range 60 μm –850 μm , were obtained by Serjeant & Harrison (2005) by modeling the spectral energy distributions (SEDs) of all 15,411 *IRAS* PSCz galaxies (Saunders et al. 2000). The SEDs were constrained by all available far-infrared and sub-mm colour-colour relations from the SLUGS and elsewhere. The *Herschel* surveys have allowed the first determinations of local luminosity functions at 250, 350 and 500 μm based on complete samples of sub-mm selected galaxies (Dye et al. 2010, Vaccari et al. 2010, Dunne et al. 2011). The results are in generally good agreement with the estimates by Serjeant & Harrison (2005).

The *Planck* (Planck Collaboration I, 2011) surveys have allowed the construction of the first all-sky catalogs homogeneously selected at several wavelengths from 350 μm to 1 cm, the Early Release Compact Source Catalog (ERCSC; Planck Collaboration VII, 2011). At sub-mm wavelengths the dominant population of extragalactic sources consists of nearby dusty galaxies, mostly at distances $\lesssim 100$ Mpc, all with spectroscopic redshift measurements. These are almost ideal characteristics for estimating local luminosity functions. In contrast, because of the much smaller covered areas, to get sufficient statistics with *Herschel* surveys it is necessary to select galaxies up to $z = 0.1$ – 0.2 where evolutionary effects may be non-negligible, requiring model-dependent corrections. In addition, for many relatively distant galaxies only photometric redshifts are available.

On the other hand, very low redshift galaxy samples ($z \ll 0.1$), like those provided by *Planck* surveys, have their own drawbacks that must be dealt with carefully. First, proper motions can give large contributions to the measured redshifts, hence making them unreliable as distance indicators; redshift-independent distance indicators need then to be used as far as possible. Second, we live in the outskirts of the Virgo super-cluster implying that *Planck* samples contain strong density inhomogeneities, while the standard method to estimate the luminosity function [the $1/V_{\text{max}}$ method (Schmidt 1968)] assumes a uniform distribution of galaxies. Although the effect of inhomogeneities is substantially mitigated by the (almost) full sky coverage, it must be taken into account.

In this paper we exploit the *Planck* ERCSC to estimate the local luminosity functions of star-forming galaxies at 217 GHz (1382 μm), 353 GHz (850 μm), 545 GHz (550 μm) and 857 GHz (350 μm). Our analysis provides a useful complement to the recent paper by the *Planck* collaboration (Planck Collaboration VII, 2012), in which the sub-millimetre to millimetre number counts and spectral indices of dust-dominated galaxies, as well as of extragalactic radio sources, selected in the ERCSC are presented.

The paper is organized as follows. In §2 we describe the selection of the samples, their completeness and the correc-

tion of the *Planck* fluxes for CO-line emission. In §3 we deal with the methodology used to measure the luminosity function and present the results, that, in §4, are compared with earlier estimates. Our main conclusions are summarized in §5. Throughout this paper we adopt a flat cosmology with $\Omega_{0,m} = 0.27$ and $H_0 = 70 \text{ km s}^{-1} \text{ Mpc}^{-1}$.

2 THE SAMPLES

2.1 The ERCSC

The *Planck* ERCSC lists all high-reliability sources, both Galactic and extragalactic, based on mapping the entire sky once and 60% of the sky a second time in 9 frequency bands centered at 30, 44, 70, 100, 143, 217, 353, 545 and 857 GHz. At the frequencies of interest here, the Full Width at Half Maximum (FWHM) of the *Planck* beam is 4.68 arcmin at 217 GHz (1382 μm), 4.43 arcmin at 353 GHz (850 μm), 3.80 arcmin at 545 GHz (550 μm) and 3.67 arcmin at 857 GHz (350 μm) (Planck Collaboration I, 2011). Below 353 GHz the detected extragalactic sources are mostly radio loud Active Galactic Nuclei (AGNs), while at frequencies ≥ 353 GHz they are mostly dusty galaxies (Planck Collaboration XIII 2011; Planck Collaboration VII 2012). Since we are interested in the latter objects we focus our analysis on the three highest frequency *Planck* channels although we could also derive an estimate, over a limited luminosity range, of the luminosity function of dusty galaxies at 217 GHz.

The ERCSC offers, for each source, four different flux density measurements (Planck Collaboration VII 2011). One is that determined by the source detection algorithm (FLUXDET); the others are based on aperture photometry (FLUX), on fitting the source with the *Planck* point spread function at the location of the source (PSFFLUX), and on fitting the source with an elliptical Gaussian model (GAUFLUX). As stated in the Explanatory Supplement to the *Planck* ERCSC (Planck Collaboration 2011) the ERCSC flux density values need to be corrected by factors depending on the spectral shape of the sources. We have adopted the multiplicative correction factors appropriate for a spectral index $\alpha = 3$ ($F_\nu \propto \nu^\alpha$), i.e. 0.896, 0.887, 0.903 and 0.965 at 217, 353, 545 and 857 GHz, respectively, as given in the Explanatory Supplement.

It is important to remember that, in building the ERCSC, the emphasis was more on source reliability than on photometric accuracy or completeness (Planck Collaboration VII 2011), and the absolute calibration of flux-density values was required to be accurate to within about 30%, although the signal-to-noise of the sources are much higher. To investigate the best *Planck* flux density measurements and their photometric quality we have exploited *Herschel* flux density measurements from the *Herschel* Reference Survey (HRS; Boselli et al. 2010), as given in Ciesla et al. (2012; 149 galaxies at 857 GHz and 86 at 545 GHz), from the Key Insights on Nearby Galaxies Survey, KINGFISH (Dale et al. 2012, 33 galaxies at 857 GHz and 33 at 545 GHz), from the *Herschel* Virgo Cluster Survey (HeViCS; Davies et al. 2012, 39 galaxies at 857 GHz and 19 at 545 GHz), and from the *Herschel* Astrophysical Terahertz Large Area Survey (H-ATLAS; Eales et al. 2010) as given in Herranz et al. (2012, 11 galaxies at 857 GHz and 6 at 545 GHz). We have applied

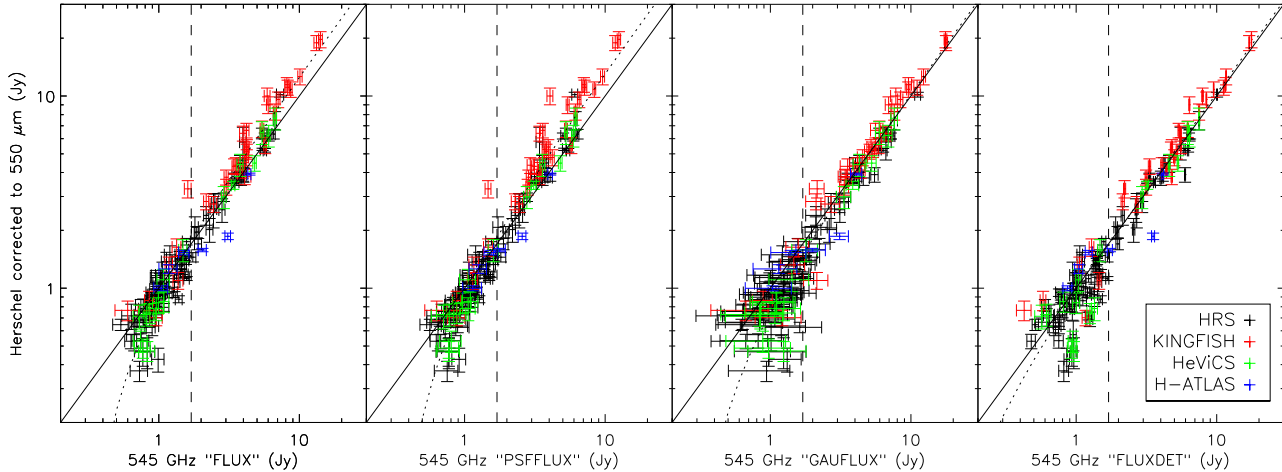


Figure 1. Comparison of the 4 *Planck* flux density estimations at 545 GHz (550 μm) with *Herschel* measurements at 500 μm , colour corrected to 550 μm using the spectral index determined from the *Planck* measurements for each individual galaxy at 545 and 857 GHz. The HRS flux densities (black) are from Ciesla et al. (2012), Kingfish flux densities (red) are from Dale et al. (2012), the HeViCS flux densities are from Davies et al. (2012) and the H-ATLAS flux densities (blue) are from Herranz et al. (2012). The 4 panels refer to the 4 estimates provided in the ERCSC: 'FLUX', 'PSFFLUX', 'GAUFLUX' and 'FLUXDET' (from left to right), see text. The black solid lines correspond to a *Herschel/Planck* flux density ratio of 1. The dotted curves are the linear least squares fits [eq. (1)] for the full sample (coefficients A and B in Table 1) and the vertical dashed lines correspond to the adopted 80% completeness limit (see § 2.3).

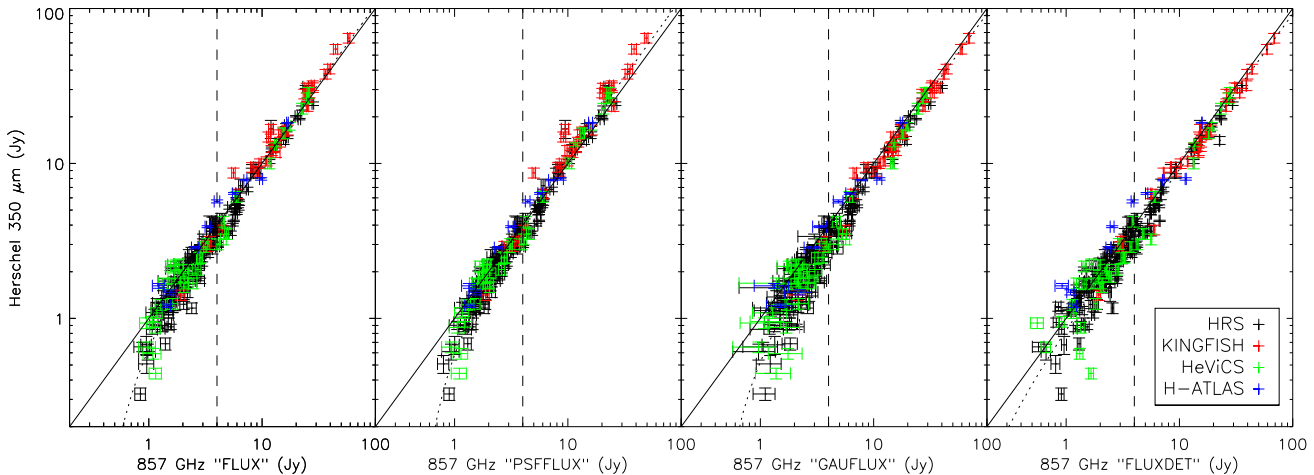


Figure 2. Comparison of the 4 *Planck* flux density estimations at 857 GHz (350 μm) with *Herschel* measurements at the same frequency. The symbols and the lines have the same meaning as in Fig. 1.

to the *Herschel* flux density measurements colour corrections by factors of 1.004 and 1.02 at 350 and 500 μm , respectively, appropriate for extended sources with dust temperature of 20 K and dust emissivity index $\beta = 1.5$ (Table 2 of Ciesla et al. 2012).

The *Planck* 857 GHz and *Herschel* 350 μm bands have (by design) very similar central wavelengths and the colour corrected flux densities in these bands can be compared directly. The *Planck* 545 GHz (=550 μm) and *Herschel* 500 μm bands, on the other hand, are slightly offset. In order to compare the measurements in these two nearby bands a small colour correction is needed. In order to do this we extrapolate the *Herschel* flux densities to 550 μm using the spectral index for each source as determined by the measured

Planck flux densities at 857 and 545 GHz. For sources missing *Planck* measurements at one of these 2 frequencies we have adopted the average value found for the others, i.e. $\alpha = 2.7$. The results of these flux comparisons are shown in Figs. 1 and 2.

In doing this exercise we need to take into account that *Planck* measurements may suffer from blending of close-by sources, individually detected by *Herschel*. Visually inspecting each HRS galaxy associated to a *Planck* source, Ciesla et al. (2012) found potential contamination of 11 sources out of the 155 in common with *Planck* at 350 μm . Two *Planck* sources in the HeViCS survey, out of 60 observed, are found to be blends of galaxy pairs well resolved by *Herschel*: NGC 4298 + NGC 4302 and NGC 4567/8 (Davies et

al. 2012). One additional blend of two comparably bright galaxies (NGC 3719 + NGC 3720) was found by Herranz et al. (2012), out of 12 detected galaxies in the H-ATLAS equatorial fields. In these cases, the *Planck* source has been split into its components and we have adopted the *Herschel* flux densities of the individual galaxies at 350 and 500 μm (the latter rescaled to 550 μm). At longer wavelengths we have assigned to the two components flux density values whose sum equals the measured *Planck* flux density at that wavelength and whose ratio is equal to the one measured by *Herschel* at 500 μm . A visual inspection of optical images of the ERCSC sources without *Herschel* observations showed that only few per cent of them are associated to galaxy pairs. Therefore we conclude that source blending is not a major problem for estimates of the luminosity functions using *Planck* data.

We have performed a linear fit to the data in Figs. 1 and 2:

$$F_{\text{Herschel}} = A + B \times F_{\text{Planck}}. \quad (1)$$

The derived coefficients are listed in columns 2 and 3 of Table 1. As the ERCSC is expected to suffer from the Eddington (1913) bias at low flux densities, we have repeated the calculation of the linear fits restricting ourselves to the sub-samples of galaxies with $F_{\text{Planck}} > 3 \text{ Jy}$ at 857 GHz (350 μm), and with $F_{\text{Planck}} > 2 \text{ Jy}$ at 545 GHz (550 μm); the corresponding coefficients, A_* and B_* , are also given in Table 1. The rms fractional differences between *Planck* and *Herschel* flux densities, $\text{rms} = (1/\sqrt{N})[\sum_{i=1}^N (F_{\text{Planck},i} - F_{\text{Herschel},i})^2 / F_{\text{Planck},i}^2]^{1/2}$, for the two bright sub-samples are given in the last column of the Table.

From this analysis we draw the the following conclusions:

- As expected, all the 4 *Planck* measurements are systematically higher than the *Herschel* measurements for flux densities below $\lesssim 1.5 \text{ Jy}$ (the best fit values of the coefficient A are all negatives). This is likely due to the Eddington (1913) bias.
- At 857 GHz, FLUX is the *Planck* flux density measurement most consistent with *Herschel* data, as it provides the lowest dispersion around the *Herschel* measurements. However, compared to GAUFLUX, it seems to slightly underestimate the flux density of the brightest fluxes, corresponding to resolved nearby galaxies. This is probably due to the failure of the adopted point source model.
- At 545 GHz the *Planck* flux density estimates most consistent with *Herschel* results are GAUFLUX and FLUXDET, the former showing a slightly lower dispersion of *Planck* to *Herschel* flux density ratios for the bright sub-sample. Both FLUX and PSFFLUX underpredict the flux densities of the brightest (i.e. resolved) galaxies, with derived values of the slope B significantly higher than 1.

In the light of these considerations, we took FLUX as our reference *Planck* flux density measurement at 857 GHz and used eq. (1) with the values of A and B taken from Table 1 (first and second columns) to bring it in statistical agreement with *Herschel* measurements before deriving the rest-frame luminosities. At 545 GHz we adopted the GAUFLUX values corrected again according to eq. (1). At 353 GHz and 217 GHz there are no *Planck*-independent flux density measurements for a statistically significant number of local

	A (Jy)	B	A_* (Jy)	B_*	rms _*
857 GHz (350 μm)					
FLUX	−0.4197	1.0533	−0.7933	1.0805	0.1529
PSFFLUX	−0.5847	1.1645	−1.1290	1.2115	0.2121
GAUFLUX	−0.4073	0.9297	−0.5789	0.9326	0.1990
FLUXDET	−0.0876	0.9241	−0.4118	0.9405	0.1665
545 GHz (550 μm)					
FLUX	−0.4129	1.2904	−1.0541	1.3934	0.5927
PSFFLUX	−0.4660	1.3499	−0.8308	1.4079	0.7690
GAUFLUX	−0.2999	1.0503	−0.6107	1.0979	0.3880
FLUXDET	−0.0991	1.0440	−0.3830	1.1020	0.4208

Table 1. Coefficients of the linear least square relation between *Planck* and *Herschel* flux densities at 857 and 545 GHz for the whole sample shown in Figs 1 and 2 (A , B) and for the sub-samples with flux density greater than 3 Jy at 857 GHz and greater than 2 Jy at 545 GHz (A_* and B_*). Also shown are the rms fractional differences between *Planck* and *Herschel* flux densities for the bright sub-samples (rms_{*}).

galaxies in the *Planck* sample (in fact, only a few galaxies in our 353 GHz *Planck* sample have SCUBA imaging data from SLUGS). Since the luminosity function is derived for a sub-sample of relatively bright galaxies (see § 2.3), and given that GAUFLUX seems to perform quite well at both 857 and 545 GHz for the sub-mm brightest galaxies, we have decided to use that flux density estimate at 353 and 217 GHz.

2.2 Selection of star-forming galaxies

The first step towards the selection of dusty galaxy samples is the identification and removal of Galactic and AGN-dominated sources. The contamination by Galactic sources was minimized by masking regions heavily affected by Galactic emissions. Planck Collaboration VII (2012) used still unpublished *Planck* maps to create the mask. Here we rely instead on the 100 μm map of Schlegel, Finkbeiner, & Davis (1998) that we smoothed with a beam of FWHM = 180'. Pixels in the upper intensity quartile (in the unsmoothed map) are discarded as being contaminated by Galactic emission. The masked region includes 29.1% of the sky, thus leaving an area of 29,250 deg² for the measurement of the luminosity function. The numbers of *Planck* detections within that area are listed in Table 2.

In order to help identifying Galactic sources, the ERCSC includes two flags for each source: 'EXTENDED' and 'CIRRUS'. The flag EXTENDED is set to 1 when the square root of the product of the measured major and minor axes of the source is 1.5 times greater than the square root of the product of the major and minor axes of the estimated *Planck* point spread function at the location of the source. Otherwise the flag is set to 0. Given the arcmin size of the *Planck* beam in the frequency range 857 to 217 GHz (see § 2.1), detections with EXTENDED=1 are likely to be associated with structure in the Galactic interstellar medium (Herranz et al. 2012). The numbers of *Planck* detections with EXTENDED=0 within the selected area are reported in Table 2, together with that of sources

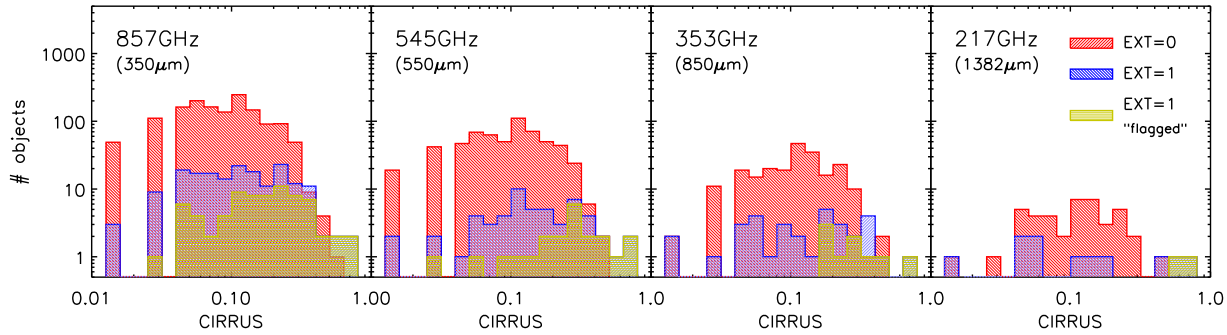


Figure 3. Histogram of the flag CIRRUS values for the local galaxies in our sample with EXTENDED=0 (red histogram) and with EXTENDED=1 (blue histogram). The sub-sample of galaxies with EXTENDED=1 that were flagged as “contaminated by cirrus” is shown by the yellow histogram.

with EXTENDED=1 within the same area. The flag ‘CIRRUS’ quantifies how crowded the region around each *Planck* detection is, by providing the number of sources within a 2° radius from the source, in raw 857 GHz catalogues. The number is normalized to a peak value of unity. The normalization factor is obtained from the number density of sources in the Large Magellanic Cloud region where the highest concentration of 857 GHz sources is observed. High values of this flag, e.g. $\text{CIRRUS} \gtrsim 0.125$ (Herranz et al. 2012), may indicate that the detection has a Galactic origin or, if not, that the flux measurement is severely contaminated by Galactic dust emission. There are exceptions. In fact, some nearby galaxies have either EXTENDED=1 or CIRRUS>0.125 or both. One example is M81, which has EXTENDED=1 (at 217 GHz) and CIRRUS=0.434. Planck Collaboration XVI (2011) found that about 20% of the objects in their sample of robustly identified nearby galaxies are classified as extended in the ERCSC. The most effective way to separate local galaxies from Galactic sources would be to visually inspect optical to infrared imaging data for all the *Planck* detections. This is the kind of approach we have decided to adopt here. However, as this method is time consuming, we have carried it out on all the detections with EXTENDED=0 and only on a sub-sample with EXTENDED=1 (as only a small fraction of local galaxies are expected to be flagged as extended in the ERCSC). We have decided to not exploit the flag CIRRUS for reasons explained in § 2.2.2 where we also describe the definition and the analysis of the sub-sample with EXTENDED=1. We first focus on the catalogue with EXTENDED=0.

2.2.1 Sample with EXTENDED=0

In order to pick up radio loud AGNs we have exploited the strong difference of their spectral shape compared with that of dusty galaxies at mm and sub-mm wavelengths. In this wavelength range the spectral index (α , with $F_\nu \propto \nu^\alpha$) of radio-loud AGNs is generally $\lesssim 0$ while that of dusty galaxies is $\gtrsim 2.5$. Since the former are increasingly important with decreasing frequency, we have first focused on the 217 GHz sample and cross-correlated it with the ERCSC at 100 GHz in order to estimate the 100-to-217 GHz spectral index. We found 309 (out of 473) sources with $F_{100}/F_{217} > 1$ and dropped them from the sample as being dominated by

ν_{obs} (GHz)	217	353	545	857
λ_{obs} (μm)	1382	850	550	350
n_{tot}	964	1762	3781	6004
$n_{\text{EXT}=0}$	473	584	946	1887
$n_{\text{EXT}=1}$	491	1178	2835	4117
$n_{\text{EXT}=0,\text{local}}$	42	220	598	1463
$n_{\text{EXT}=1,\text{local}}$	11(9)	33(20)	55(21)	182(56)

Table 2. Total number of ERCSC sources, n_{tot} , outside the adopted Galactic mask. Also shown are: the numbers of sources with EXTENDED=0 ($n_{\text{EXT}=0}$) and EXTENDED=1 ($n_{\text{EXT}=1}$), the number of identified galaxies at $z < 0.1$ with EXTENDED=0 ($n_{\text{EXT}=0,\text{local}}$) and with EXTENDED=1 ($n_{\text{EXT}=1,\text{local}}$). In parenthesis are the numbers of the galaxies with EXTENDED=1 and $z \leq 0.1$ that were kept for estimating the luminosity function (see text for details).

radio emission. Note that this approach is different from that adopted by Planck Collaboration VII (2012), where the 857-to-545 GHz and 545-to-353 GHz flux density ratios were used to separate radio sources from galaxies whose spectral energy distribution is dominated by thermal dust emission.

As a counter-check, we cross-correlated our 217 GHz sample with the CRATES catalogue (Healey et al. 2007) adopting a search radius of $3'$. This radius is somewhat larger, for these *Planck* channels, than the $1/2$ FWHM of the *Planck* beam found by Planck Collaboration XIV (2011) to be sufficient to locate any related source. CRATES provides a nearly uniform extragalactic ($|b| > 10^\circ$) coverage for flat-spectrum ($\alpha > -0.5$) radio sources brighter than 65 mJy at 4.8 GHz. As expected, since radio sources detected by *Planck* are generally flat-spectrum, most of the sources dropped as synchrotron dominated have a bright CRATES counterpart. The cross-correlation with CRATES however misses a bunch of very bright steep-spectrum sources (e.g. 3C 207, 3C 216, 3C 286, 3C 380) and includes some sources whose (sub)-mm emission is clearly dominated by dust (e.g. M82, M83, M104). On the whole, the cross-correlation with CRATES confirmed our previous conclusions and did not reveal any misclassified source.

The remaining $473 - 309 = 164$ sources were inspected individually. We used the interactive software sky atlas AI-

adin (Bonnarel et al. 2000) to inspect the available optical to far-infrared imaging data (e.g. IRAS maps) and to query the NASA/IPAC Extragalactic Database (NED)¹ around the position of each source. We removed all those objects that did not have a nearby ($z < 0.1$) galaxy within the adopted search radius but, instead, satisfied one (or more) of the following conditions: (i) association with an extended clumpy/filamentary structure in the IRAS maps (if available); (ii) presence of a bright (i.e. $F_{1.4\text{GHz}} > 0.1$ Jy) radio source; (iii) presence of a group/cluster of galaxies (examples are Abell 2218 and the Bullet cluster); (iv) the *Planck* sources is un-detected in IRAS maps. The last condition is meant to eventually identify and remove false *Planck* detections that may have been induced by background fluctuations, which are expected to be significant in low-resolution surveys (see e.g. Negrello et al. 2004, 2005). We identified 122 objects obeying at least one of the conditions listed above (we will refer to them as “contaminants”). Removing those sources from the catalogue left us with a final, cleaned, sample of 42 local galaxies at 217 GHz with EXTENDED=0, all being either Messier objects or galaxies listed in the New General Catalogue (NGC). We then moved to the 353 GHz sample and cross-correlated it with the 217 GHz catalogue, using a 3' search radius. We removed all the “contaminants” in common with the 217 GHz sample and kept all the sources that were identified as local galaxies at that frequency. We then inspected each of the remaining unclassified *Planck* detections individually, in Aladin, and removed from the sample all those objects satisfying at least one of the conditions previously illustrated. We followed the same approach at 545 and at 857 GHz after cross-correlating the catalogues with the lower frequency samples in order to exploit all the information already in hand.

The whole cleaning process, performed on the catalogue of *Planck* detections with EXTENDED=0, produced a sample of 220 local galaxies at 353 GHz, 598 at 545 GHz, and 1463 at 857 GHz (see Table 2), the majority of which are either Messier or NGC objects. The visual inspection of multi-wavelength ancillary data for each individual object minimized the risk of misidentifications and automatically provided, through the NED, the information on the redshift-independent measurements of distance, needed to derive the local luminosity function.

2.2.2 Sample with EXTENDED=1

Table 2 shows that, particularly at 857 GHz and 545 GHz, the *Planck* detections with EXTENDED=1 are a factor $\gtrsim 2$ more abundant than those with EXTENDED=0. Visually inspecting all those sources would be a very inefficient method to identify local galaxies, as the majority of the *Planck* detections with EXTENDED=1 are expected to be Galactic. Therefore we have first reduced the sample by performing an automatic cross-matching with the NED and by retaining for inspection only the *Planck* detections that happen to have at least one source with a measured redshift $z < 0.1$ within a distance of 3'. A galaxy like the Milky Way, with a linear size of ~ 30 kpc, would be assigned EXTENDED=1 for distances $\lesssim 20$ Mpc or, equivalently, for

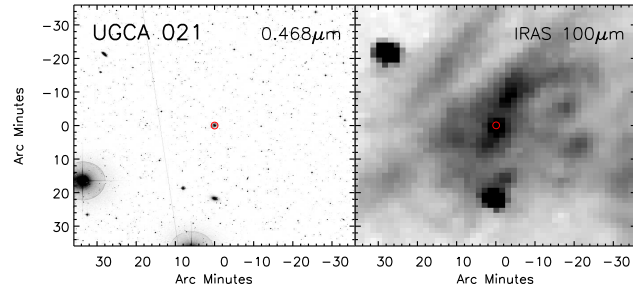


Figure 4. Postage stamp image of the galaxy UGCA-021 ($z = 0.006622$), at $0.468 \mu\text{m}$ (left-hand panel) and at $100 \mu\text{m}$ (right-hand panel). This galaxy, indicated by the red circle, is flagged as extended in the ERCSC at 545 GHz and has CIRRUS=0.094. However the IRAS map shows that it lies behind a prominent structure in the Galactic interstellar medium.

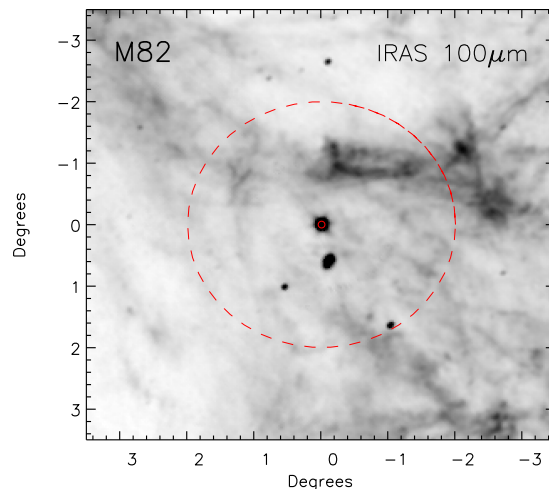


Figure 5. Postage stamp image of the galaxy M82 ($z = 0.00068$), at $100 \mu\text{m}$. The galaxy, indicated by the red circle, has EXTENDED=0 at 545 GHz and CIRRUS=0.5. The dashed red circle marks the region of 2° radius centered on the galaxy. The high value of the flag CIRRUS is likely due to the presence, in the vicinity, of a prominent structure in the Galactic interstellar medium, seen in the top-right corner of the image.

redshifts $z \lesssim 0.005$. Therefore our choice of an upper limit of 0.1 in redshift is very conservative. The numbers of objects left over after the cross-matching with the NED are reported in Table 2. Upon visual inspection of each individual source in Aladin, to identify and remove radio sources and Galactic objects, we flagged as “contaminated by cirrus” those galaxies that happened to lie behind a prominent filamentary structure in the IRAS $100 \mu\text{m}$ map. These galaxies are likely to have their *Planck* flux density measurements severely affected by Galactic emission and therefore we have decided to drop them from the final sample. The number of galaxies with EXTENDED=1 actually used for deriving the luminosity function is shown in parenthesis in Table 2. One might have used the flag CIRRUS to identify local galaxies falling behind prominent Galactic structures, by imposing an upper limit on the CIRRUS values, for example 0.125, as

¹ <http://ned.ipac.caltech.edu/>

ν_{obs} (GHz)	λ_{obs} (μm)	n_{obj}	F_{lim} (mJy)	$\log \bar{F}$	$\sigma_{\log F}$
857	350	328	4086	2.71	0.95
545	550	234	1814	2.63	0.66
353	850	108	809	2.39	0.55
217	1382	30	497	2.27	0.44

Table 3. Flux density limits (F_{lim}) corresponding to 80% completeness and numbers of local dusty galaxies brighter than these limits, used for estimating the luminosity functions. The quantities $\log \bar{F}$ and $\sigma_{\log F}$ are the best-fit values of the parameters that define the completeness function [eq. (13)], where the flux density is in mJy.

suggested by Herranz et al. (2012). However Fig. 3 demonstrates that this approach is prone to misidentifications. In fact, the figure shows the histogram of the flag CIRRUS values for the sample of local galaxies with EXTENDED=0 (in red) and that with EXTENDED=1 (in blue), while the yellow histogram refers to the sub-sample of galaxies with EXTENDED=1 that were flagged as “contaminated by cirrus”. While the latter objects are indeed those with the highest CIRRUS values at 217 GHz and 353 GHz, the situation becomes less well defined at shorter wavelengths where several of them turn out to have CIRRUS $\lesssim 0.1$. One example is shown in Fig. 4. On the other hand there are some nearby galaxies that, upon inspection of the IRAS 100 μm maps, do not seem to be contaminated by Galactic cirrus but, nevertheless, have CIRRUS > 0.2 . Examples are M64, M82, M90, NGC7392. As illustrated in Fig. 5 for M82, the high CIRRUS value in these sources is probably due to the presence, in the vicinity of the galaxy (i.e. within 2°) but not directly on top of it, of a prominent structure in the Galactic interstellar medium.

2.3 Number counts and completeness

The completeness of our samples of local dusty galaxies can be tested by means of the differential source counts. Apart from the effect of inhomogeneities in the spatial distribution of galaxies, the counts must have an Euclidean slope (i.e. $dN/dS \propto S^{-2.5}$) and the onset of incompleteness is indicated by a decline below the Euclidean power law. The counts were estimated using a bootstrap resampling method that allows us to account for the uncertainties in the flux density measurements. In practise we have generated 1000 simulated catalogues by resampling, with repetitions, the input catalogue. In each simulation we have assigned to each source a flux density value randomly generated from a Gaussian probability distribution with a mean equal to the measured flux density and dispersion σ equal to the associated error. The distribution of source flux densities derived from the simulations were binned into a histogram and the mean value in each bin was taken as the measurement of the number count in that bin, once divided by the bin size and by the survey area. The errors on the number counts were derived assuming a Poisson statistic, according to the prescriptions of Gehrels (1986).

The results are shown in Fig. 6 in the form of Euclidean normalized differential number counts and in Fig 7

as integral number counts. As expected, the counts exhibit an Euclidean slope at the brightest flux densities, followed by a downturn (or a flattening in the cumulative counts), which is due to the onset of incompleteness in the sample. The counts are compared with those estimated for dust-dominated galaxies by Planck Collaboration VII (2012), who used (i) a Galactic mask derived from *Planck* data, (ii) an automatic procedure to identify dusty galaxies based on *Planck* colours, (iii) completeness corrections obtained from extensive simulations, (iv) FLUX as the reference flux density measurement at all frequencies. The agreement is generally good, particularly at 857 and 545 GHz. At 353 GHz and at 217 GHz the faintest counts produced by the *Planck* collaboration lie above the extrapolation of our measurements. This may be due to the appearance of a strongly evolving population with a “super-Euclidean” slope. However the possibility of either an overestimate of the correction for incompleteness or of a contamination of the sample e.g. by Galactic and/or radio sources can hardly be ruled out at this stage.

Fitting the brightest part of the Euclidean normalized counts (i.e. above 5, 2, 0.8, and 0.5 Jy at 857, 545, 353 and 217 GHz, respectively; these flux density limits are indicated by the vertical dotted lines in Figs. 6 and 7) with a straight horizontal line we get 486 ± 32 , 103 ± 8 , 14 ± 1 and $1.7 \pm 0.4 \text{ Jy}^{1.5} \text{ sr}^{-1}$ at 857, 545, 353 and 217 GHz, respectively. These values are fully consistent with those estimated by Planck Collaboration VII (2012) for dusty galaxies: 627 ± 152 , 125 ± 15 , and 15 ± 6 at 857, 545 and 353 GHz, respectively (at 217 GHz the *Planck* collaboration provides the Euclidean plateau level for synchrotron dominated galaxies only).

The completeness as a function of the flux density was estimated as the ratio of the observed counts to those expected from the best-fit Euclidean counts. It is well approximated by an error function

$$C(F) = \text{erf}[(\log F - \log \bar{F})^2 / \sigma_{\log F}^2], \quad (2)$$

where $\log \bar{F}$ and $\sigma_{\log F}$ are free parameters whose best fit values for each *Planck* channel are given in Table 3. For the estimation of the luminosity functions we adopted the flux density limits corresponding to an 80% completeness. These limits are listed in Table 3 and represent *observed* flux densities, i.e. no correction for either CO-line emission (see next sub-section) or Eddington-bias [i.e. eq. (1)] was applied when measuring the number counts. In fact those corrections are only introduced when calculating the rest-frame luminosities. In the same table we also give the corresponding numbers of local dusty galaxies used to estimate the luminosity functions. All of them have a spectroscopic redshift. The completeness curves [eq. (13)] are also used to compute the weight factor for each source, $w_i = 1/C(F_i)$, F_i being the flux of the i -th galaxy, to be used in the estimate of the luminosity function [see eq. (5) and eq. (13)].

By comparing our number counts with those predicted by Serjeant & Harrison (dashed lines in Figs. 6 and 7), we find that the latter lie significantly below the former, particularly at the longest wavelengths, implying that the Serjeant & Harrison local luminosity functions were also underestimated. This is not surprising since the Serjeant & Harrison estimates were obtained extrapolating the IRAS 60 μm data to 850 μm using the sub-millimeter/far-infrared colour re-

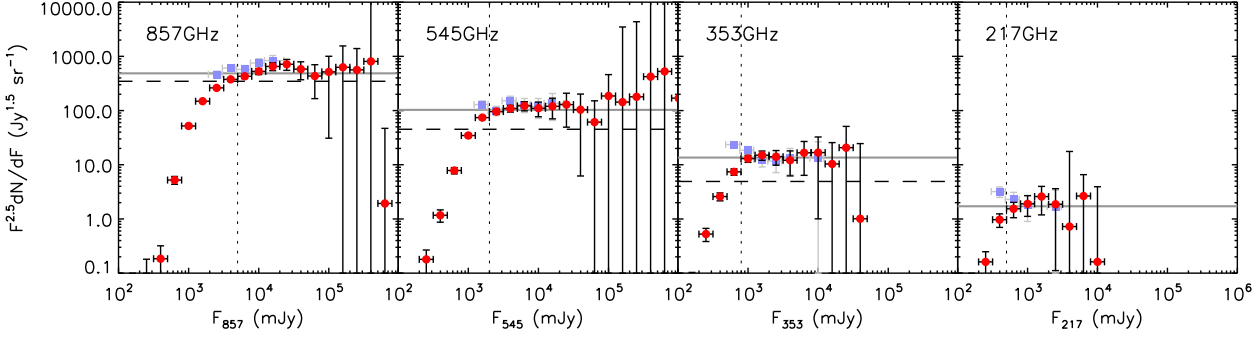


Figure 6. Euclidean normalized number counts of local star-forming galaxies at 857 GHz ($350\,\mu\text{m}$), 545 GHz ($550\,\mu\text{m}$), 353 GHz ($850\,\mu\text{m}$) and 217 GHz ($1382\,\mu\text{m}$) (red dots with error bars). Also shown, for comparison, are the counts estimated by Planck Collaboration VII (2012; blue squares, corrected for incompleteness), as well as the predictions by Serjeant & Harrison (2005; dashed lines). The thick grey line is the result of the fit to the data points with flux density above the value indicated by the vertical dotted line, assuming that the differential counts have an Euclidean slope.

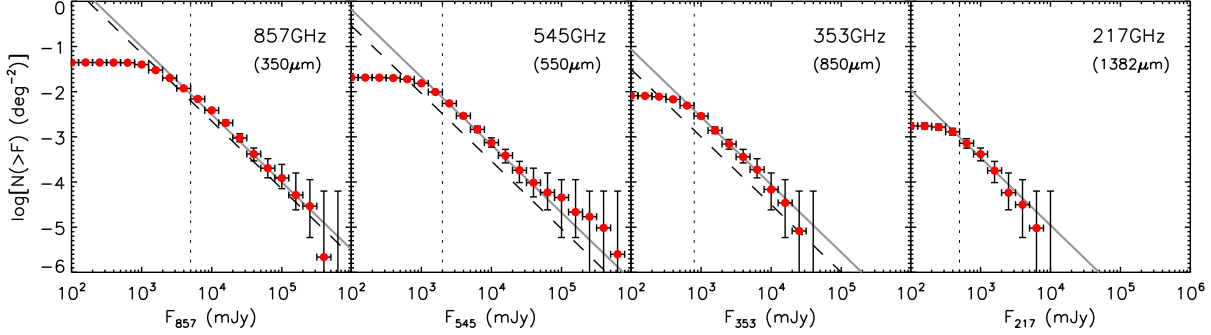


Figure 7. Integral number counts of local star-forming galaxies at 857 GHz ($350\,\mu\text{m}$), 545 GHz ($550\,\mu\text{m}$), 353 GHz ($850\,\mu\text{m}$) and 217 GHz ($1382\,\mu\text{m}$) (red dots with error bars). The dashed line is the prediction by Serjeant & Harrison (2005). The thick grey line represents the integral number counts derived from the fit to the bright tail of the differential counts shown in Fig. 6.

$\log[S(\text{mJy})]$	$(S^{2.5}dN/dS)_{857}$ ($\text{Jy}^{1.5}\text{sr}^{-1}$)	$(S^{2.5}dN/dS)_{545}$ ($\text{Jy}^{1.5}\text{sr}^{-1}$)	$(S^{2.5}dN/dS)_{353}$ ($\text{Jy}^{1.5}\text{sr}^{-1}$)	$(S^{2.5}dN/dS)_{217}$ ($\text{Jy}^{1.5}\text{sr}^{-1}$)
2.8	-	-	-	1.6 ± 0.5
3.0	-	-	13.0 ± 1.9	1.9 ± 0.7
3.2	-	-	15.0 ± 2.9	2.6 ± 1.4
3.4	-	96 ± 10	14.0 ± 4.2	1.9 ± 1.8
3.6	-	109 ± 15	12.3 ± 6.0	0.7 ± 17.2
3.8	429 ± 41	121 ± 24	17 ± 10	2.8 ± 4.1
4.0	528 ± 67	109 ± 33	17 ± 16	-
4.2	652 ± 108	121 ± 50	10 ± 15	-
4.4	715 ± 164	126 ± 78	19 ± 29	-
4.6	582 ± 212	103 ± 97	-	-
4.8	434 ± 268	57 ± 1336	-	-
5.0	517 ± 486	184 ± 272	-	-
5.2	630 ± 929	-	-	-
5.4	563 ± 830	-	-	-
5.6	-	-	-	-

Table 4. Euclidean normalized number counts of local star-forming galaxies at 857 GHz ($350\,\mu\text{m}$), 545 GHz ($550\,\mu\text{m}$), 353 GHz ($850\,\mu\text{m}$) and 217 GHz ($1382\,\mu\text{m}$), for flux densities greater than the values indicated by the vertical dotted lines in Figs. 6 and 7.

lation derived from the SLUGS (Dunne et al. 2000). The latter is known to be biased against galaxies with large cold dust components (see Vlahakis et al. 2005 and the discussion in 4), which are instead readily detected by *Planck* (Planck Collaboration XVI 2011).

2.4 Correction of *Planck* fluxes for CO line emission

All the *Planck* High Frequency Instrument (HFI) bands, except that at 143 GHz, include emission from the CO molecule in low redshift galaxies. This emission is a contaminant for our purposes as we are concerned with the dust continuum emission from star forming galaxies. Since most of the sources in our samples lack CO data and we are dealing with the properties of the population as a whole, we apply to the *Planck* fluxes average correction factors for contamination from the various CO lines before deriving the corresponding rest-frame luminosities.

The correction factors are based on the correlation between the total far-infrared luminosity (L_{FIR}) and the CO line emission, L_{CO} , and specifically on the correlation presented by Genzel et al. (2010) who found a close to linear relation between L_{CO} and $L_{\text{FIR}}(50\text{--}300\mu\text{m})$ for normal star-forming galaxies with an average ratio $L_{\text{FIR}}/L'_{\text{CO}(1-0)} = 27 L_{\odot}/(\text{K km s}^{-1} \text{pc}^2)$. The units of $L'_{\text{CO}(1-0)}$, ($\text{K km s}^{-1} \text{pc}^2$) can be converted to solar luminosities with the relation given by Solomon et al (1997), $L_{\text{CO}}/L_{\odot} = 3.2 \times 10^{-11} (\nu_{\text{rest}}/\text{GHz})^3 (L'_{\text{CO}}/(\text{K km s}^{-1} \text{pc}^2))$, to find $L_{\text{FIR}}/L_{\text{CO}(1-0)} = 5.55 \times 10^5$ with both luminosities in solar units. Although there is evidence that the correlation is different for merger systems with high values of L_{FIR} (see e.g. Daddi et al. 2010) we did not feel that there were enough such systems in our sample to justify refinement of the corrections.

In order to correct the *Planck* fluxes contaminated by CO($J = 2 - 1$) (217 GHz band), CO($J = 3 - 2$) (353 GHz band), and CO($J = 5 - 4$) (545 GHz band)², we assumed fixed line strength ratios. The CO($J = 2 - 1$)/($J = 1 - 0$) ratio in antenna temperature units, r_{21} , was taken as 0.8, which is a value typical of nearby galaxies (Leroy et al. 2009). The CO($J = 3 - 2$)/($J = 1 - 0$) ratio, r_{31} , was taken as 0.66 based on the results of Yao et al. (2003). A similar median value, $r_{31,\text{median}} \simeq 0.7$, was found by Mao et al. (2012; their mean value is however somewhat higher, $r_{31,\text{mean}} \simeq 0.81$), while Papadopoulos et al. (2011) find $r_{31,\text{mean}} \simeq 0.49$. Finally, $r_{51} = \text{CO}(J = 5 - 4)/(\text{CO}(J = 1 - 0))$ was taken as 0.3 (Papadopoulos et al. 2011).

The procedure adopted was as follows. The IRAS 60 and 100 μm fluxes (available for all our sources) were used to calculate the FIR (50–300 μm) luminosity, L_{FIR} , in the same way as done by Genzel et al. (2010). This gives a prediction for the CO ($J=1-0$) luminosity. This was then scaled by the line ratios specified above, converted to flux units [$F_{\text{CO}(J,J-1)}/F_{\text{CO}(1-0)} = r_{J1}(\nu_{J,J-1}/\nu_{1-0})^2$], to give the luminosity in the various other CO transitions. The measured *Planck* flux density was then used with the predicted CO

flux to calculate the equivalent width of the CO line. The ratio of this width and the bandwidth of the *Planck* band (taken to be 30% of the centre frequency, as indicated in the ERCSC Explanatory Supplement) was used as a measure of the fractional contribution of the CO line to the Planck flux. The average correction factors for CO contamination were 0.91, 0.97 and 0.99 at, 217, 357 and 545 GHz, respectively. These values are consistent with the level of contamination estimated by Planck Collaboration XVI (2011).

2.5 Distances and rest-frame luminosities

Although a spectroscopic redshift is available for all the galaxies in our samples, this does not provide, in general, an accurate estimate of the source distance, as in the local Universe peculiar motions may introduce significant extra red- or blue-shifts in galaxy spectra. Redshift-independent distance estimates should therefore be used as far as possible. Such estimates are available in the NED for the majority of the galaxies in our samples: 65% of them at 857 GHz, 88% at 545 GHz, 95% at 353 GHz and 98% at 217 GHz. For the remaining galaxies, distances were computed from the redshifts, previously corrected to the reference frame defined by the Cosmic Microwave Background radiation using the NED on-line calculator³. We assigned to the redshift-dependent distances an arbitrary error of 30%. The distribution of the source distances at each frequency, shown in the top panels of Fig. 8, illustrates that these are truly local samples: the distances for the flux-limited sample used to estimate the luminosity functions are all ≤ 100 Mpc (i.e. $z \lesssim 0.02$).

The rest-frame luminosity of the i -th galaxy at the frequency of observation ν_{obs} is given by

$$L_i = \frac{4\pi d_i^2}{(1+z_i)k(z_i)} F_i, \quad (3)$$

where F_i is the source flux at $\nu = \nu_{\text{obs}}$, d_i is the source distance, z_i its redshift and $k(z_i) = L(\nu_{\text{obs}}(1+z_i))/L(\nu_{\text{obs}})$ is the k -correction. The latter is estimated using the SED of an Sd galaxy taken from the SWIRE template library⁴ (Polletta et al. 2007). Figure 9 shows the distribution of flux densities as a function of source luminosity. This is meant to illustrate the luminosity range covered by the samples of sources above the adopted flux density limit and how the luminosity bins are populated. The distribution of luminosities as a function of the source distance is shown in the lower panels of Fig. 8. In practice, the luminosity function is estimated from galaxies within a distance of 100 Mpc, as indicated by the vertical dashed line in Fig. 8.

3 LUMINOSITY FUNCTIONS

We have determined the luminosity functions using two different methods: the $1/V_{\text{max}}$ method and the parametric maximum likelihood method. Below we provide a brief description of the two approaches. The luminosity function is denoted as $\phi(L)$ and is taken to represent the comoving

² No correction was made for the CO($J = 7 - 6$) and ($J = 8 - 7$) lines that contaminate the 857 GHz band as their estimated contribution is negligible.

³ http://ned.ipac.caltech.edu/help/velc_help.html

⁴ www.iasf-milano.inaf.it/~polletta/templates/swire_templates.html

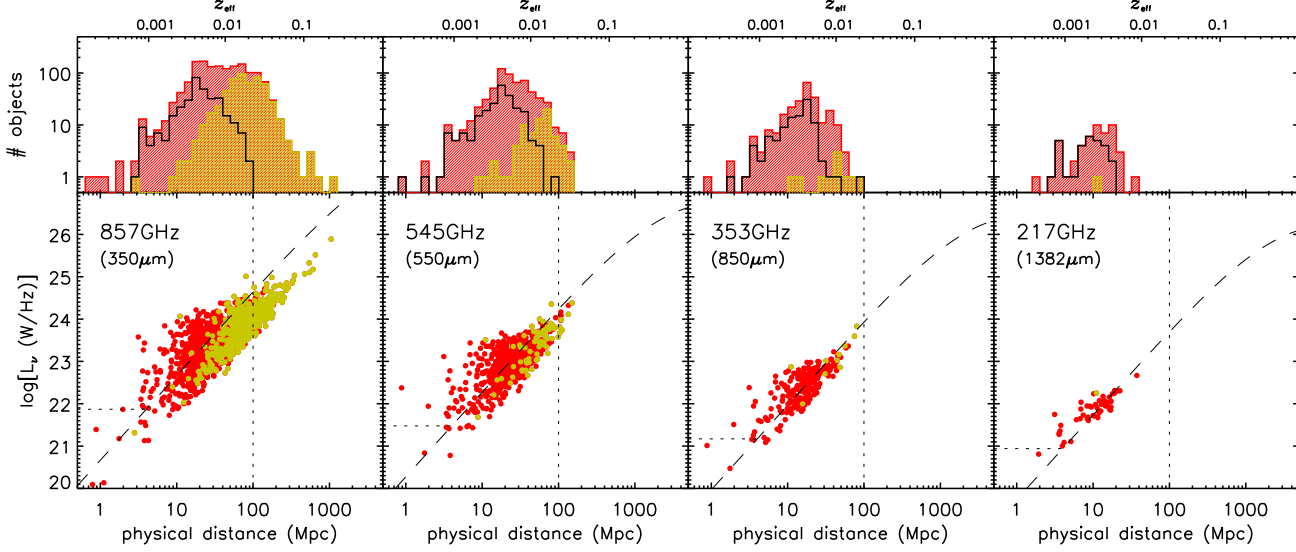


Figure 8. *Top panels:* distributions of source distances at 857 GHz (350 μm), 545 GHz (550 μm), 353 GHz (850 μm) and 217 GHz (1382 μm) for the total samples of local star-forming galaxies (red histograms), for the sub-sample without redshift-independent distance measurements (yellow histograms) and for the sub-sample with completeness above 80 % and luminosity higher than the adopted minimum value (black line). The redshift corresponding to a given distance as determined by the cosmic Hubble flow alone (i.e. the one derived by neglecting peculiar motion, that we refer to as *effective* redshift, z_{eff}) is shown in the upper x-axis. *Bottom panels:* monochromatic luminosity as a function of distance at 857, 545, 353 and 217 GHz. The colour code is the same as in the top panels. The dashed line shows the luminosity that corresponds to the adopted flux density limit as a function of distance, while the horizontal dotted line indicates the adopted minimum luminosity. Galaxies in the samples used to compute the luminosity functions have distances $\lesssim 100$ Mpc (a limit indicated by the vertical dashed line).

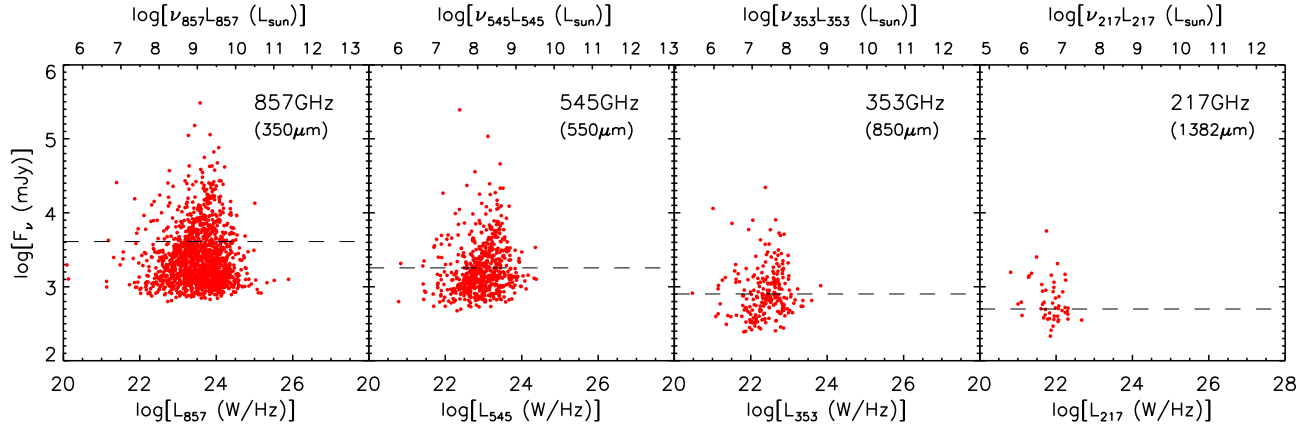


Figure 9. Measured flux density as a function of the estimated monochromatic luminosity at 857 GHz (350 μm), 545 GHz (550 μm), 353 GHz (850 μm) and 217 GHz (1382 μm). The horizontal dashed line indicates the flux limit above which the sample is 80 % complete (see § 2.3).

number density of objects per unit *logarithmic* interval in luminosity, i.e.

$$\phi(L) = \frac{dN}{dV d\log L}. \quad (4)$$

3.1 The $1/V_{\text{max}}$ method

The standard way of deriving the luminosity function is via the $1/V_{\text{max}}$ estimator (Schmidt 1968; Avni & Bahcall 1980)

$$\phi_j = \phi(L_j) = \frac{1}{\Omega \Delta \log L} \sum_i^{N_j} \frac{w_i}{V_{\text{max},i}}, \quad (5)$$

where Ω is the solid angle of the survey, w_i are the weight factors taking into account the incompleteness of the samples (see § 2.3) and the sum is over all the N_j sources with luminosity in the range $[\log L_j - \Delta \log L/2, \log L_j + \Delta \log L/2]$. The quantity $V_{\text{max},i}$ represents the (comoving) volume, per unit solid angle, enclosed by the maximum (comoving) distance, $r_{\text{max},i}$, at which the i -th object is detectable, given

$\log(L_{857})$	$\log(\phi_{857})$	$\log(L_{545})$	$\log(\phi_{545})$	$\log(L_{353})$	$\log(\phi_{353})$	$\log(L_{217})$	$\log(\phi_{217})$
22.02	$-1.32^{+0.18}_{-0.32}$	21.63	$-1.29^{+0.18}_{-0.31}$	21.32	$-1.37^{+0.19}_{-0.33}$	21.09	$-1.52^{+0.21}_{-0.44}$
22.32	$-1.55^{+0.14}_{-0.21}$	21.93	$-1.47^{+0.14}_{-0.20}$	21.62	$-1.62^{+0.15}_{-0.24}$	21.39	$-1.85^{+0.17}_{-0.29}$
22.62	$-1.75^{+0.12}_{-0.17}$	22.23	$-1.73^{+0.12}_{-0.16}$	21.92	$-1.89^{+0.13}_{-0.19}$	21.69	$-2.07^{+0.15}_{-0.23}$
22.92	$-1.94^{+0.08}_{-0.10}$	22.53	$-1.95^{+0.08}_{-0.10}$	22.22	$-2.03^{+0.09}_{-0.11}$	21.99	$-2.42^{+0.13}_{-0.18}$
23.22	$-1.99^{+0.06}_{-0.06}$	22.83	$-2.02^{+0.06}_{-0.06}$	22.52	$-2.25^{+0.07}_{-0.08}$	22.29	$-2.99^{+0.16}_{-0.24}$
23.52	$-2.24^{+0.04}_{-0.05}$	23.13	$-2.32^{+0.05}_{-0.06}$	22.82	$-2.75^{+0.08}_{-0.09}$		
23.82	$-2.71^{+0.04}_{-0.05}$	23.43	$-2.86^{+0.06}_{-0.06}$	22.12	$-3.66^{+0.13}_{-0.19}$		
24.12	$-3.37^{+0.06}_{-0.07}$	23.73	$-3.68^{+0.09}_{-0.11}$	23.42	$-4.76^{+0.24}_{-0.58}$		
24.42	$-4.17^{+0.09}_{-0.11}$	24.03	$-4.60^{+0.14}_{-0.20}$	23.72	$-5.79^{+0.37}_{-5.00}$		
24.72	$-5.22^{+0.18}_{-0.31}$	24.33	$-5.74^{+0.27}_{-0.92}$				

Table 5. Local luminosity function at 857 GHz (350 μm), 545 GHz (550 μm), 353 GHz (850 μm) and 217 GHz (1382 μm) measured via the $1/V_{\text{max}}$ method, in units of $\text{Mpc}^{-3}\text{dex}^{-1}$. Luminosities are in units of W/Hz.

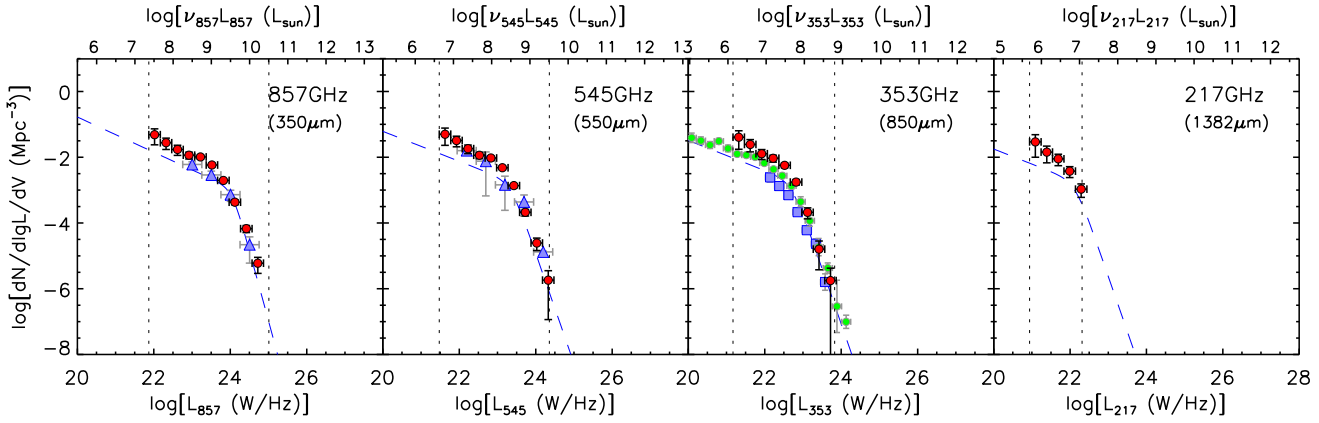


Figure 10. Local luminosity functions at 857 GHz (350 μm), 545 GHz (550 μm), 353 GHz (850 μm) and 217 GHz (1382 μm) estimated with the $1/V_{\text{max}}$ method. Also shown, for comparison, are the LF measured by Dunne et al. (2000) and Vlahakis et al. (2005) at 353 GHz (850 μm ; blue squares and green squares, respectively), and by Vaccari et al. (2010) at 350 μm and at 500 μm (blue triangles). The *Herschel* luminosities have been converted from 500 to 550 μm by assuming a spectral index $\alpha = 2.7$, the mean value found for local galaxies in the *Planck* sample. The dashed curves at 857, 545 and 353 GHz represent the predictions by Serjeant & Harrison (2005). The dashed curve at 217 GHz is the extrapolation of the Serjeant & Harrison prediction from 353 GHz assuming again a spectral index $\alpha = 2.7$. The vertical dotted lines correspond to the adopted minimum and maximum luminosities (see text).

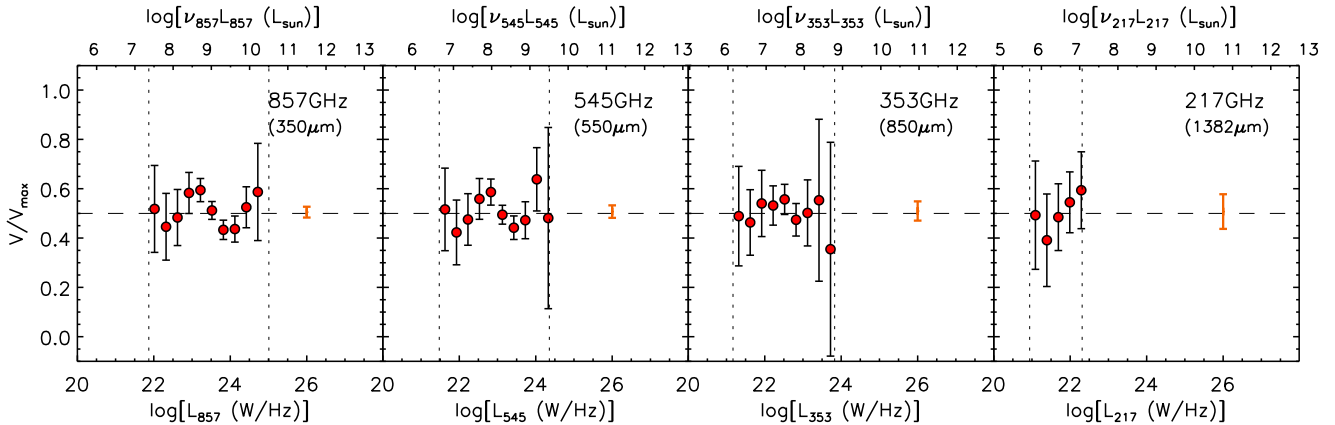


Figure 11. V/V_{max} test at 857 GHz (350 μm), 545 GHz (550 μm), 353 GHz (850 μm) and 217 GHz (1382 μm) for the flux-limited samples used to measure the luminosity function. The red dots, with error bars, are the mean V/V_{max} values for various luminosity bins while the orange error bar, here arbitrarily placed at a luminosity of 10^{26} W/Hz, represents the $\pm 1\sigma$ uncertainty on the V/V_{max} value for the whole sample. The vertical dotted lines have the same meaning as in Fig. 10.

the survey flux limit, F_{lim} , i.e., for the Euclidean geometry that applies here

$$V_{\text{max},i} = \frac{1}{3} r_{\text{max},i}^3, \quad (6)$$

where

$$r_{\text{max},i} = \frac{1}{1+z_i} \left[\frac{(1+z_i)k(z_i)L_i}{4\pi F_{\text{lim}}} \right]^{1/2}. \quad (7)$$

As stated before, when no redshift-independent distance measurements are available we used the distance computed from the redshift of the source, i.e. $d_i = cz_i/H_0$, where z_i has been corrected to the reference frame defined by the Cosmic Microwave Background radiation. However, as shown in Fig. 8, above the adopted completeness limit almost all the sources have an estimate of the distance that is independent of redshift. In order to account for uncertainties in both flux densities and distances we adopted a bootstrap resampling method to derive the luminosity function. We have generated 1000 simulated catalogues by resampling, with repetitions, the input catalogue. In each simulation, a value of the flux density and of the distance is randomly assigned to each galaxy by assuming a Gaussian distribution with a mean equal to the measured values and σ equal to the quoted errors. The rest-frame luminosities, the completeness correction factors and the maximum volumes are re-estimated from the simulated fluxes and distances. The luminosity function is then derived using eq. (5) considering only those objects with simulated flux density brighter than the adopted flux limit. Finally, the mean value of the simulated luminosity functions in each bin is taken as the estimate of the luminosity function in that bin and the rms of the distribution is taken as the uncertainty. The luminosity function estimated with the $1/V_{\text{max}}$ method is shown in Fig. 10 and tabulated in Table 5. In a flux limited survey the faintest luminosities are undersampled and, as a consequence, the luminosity function derived from the bootstrap method exhibits an artificial turn-off at faint luminosities. Therefore we have adopted, in our analysis, a minimum luminosity, L_{min} , corresponding to that of a source located 4 Mpc away from us and whose flux density is equal to the adopted flux density limit. This choice avoids the appearance of the turnoff. For similar reasons we excluded from the estimated luminosity function simulated luminosities higher than the maximum observed luminosity in the flux limited sample. The adopted minimum and maximum luminosities are indicated by the vertical dotted lines in Figs. 10–12.

The $1/V_{\text{max}}$ estimator assumes a uniform spatial distribution of sources. In general this is not the case, and the effect of large scale structures may not average away, particularly when the sampled volume is relatively small. In order to check if the distribution of the sources within each luminosity bin is consistent with uniformity, a V/V_{max} test was performed. In practice for each object within a given luminosity bin we computed the ratio between the comoving volume up to the source position, V_i , and the corresponding maximum accessible volume $V_{\text{max},i}$. For a uniform distribution $\langle V/V_{\text{max}} \rangle = 0.5 \pm 1/\sqrt{12N}$, where N is the number of sources in the bin. In order to account for the uncertainties in both flux density and distance measurements, the V/V_{max} values have been computed for each of the simulated samples used to estimate the luminosity function and then averaged

for each luminosity bin. The results are shown in Fig. 11. In each panel, the orange error bar, arbitrarily placed at a luminosity of 10^{26} W/Hz, represents the $\pm 1\sigma$ uncertainty on the $\langle V/V_{\text{max}} \rangle$ value for the whole sample. The latter is consistent with 0.5 for all the four samples, although some small deviations from 0.5 are observed in some luminosity bins at 857 GHz. We conclude that, within 2σ , the distribution of galaxies in our samples is consistent with being statistically uniform. In fact, as *Planck* covers most of the sky, local inhomogeneities are significantly diluted.

3.2 Parametric Maximum Likelihood method

A way to overcome the issue of large scale structure is to use maximum likelihood techniques, which can be either parametric or non-parametric (Sandage, Tammann & Yahil 1979; Efstathiou, Ellis & Peterson 1988; Saunders et al. 1990). The main assumption behind these methods is that the relative densities of galaxies of different luminosities are everywhere the same, and the normalization of the luminosity function is a local measure of density. In practice this means that the *observed* luminosity function can be expressed as the product of a *universal* luminosity function, independent of position, and a position-dependent term that accounts for local inhomogeneities (Yahil, Sandage & Tammann 1980; Yahil et al. 1991).

In this work we only implemented the parametric method (Sandage, Tammann & Yahil 1979, STY method), which has the advantage, compared with the non-parametric approach, that no binning of the data is required. However an analytic form of the luminosity function must be assumed. We adopt a double power-law functional form:

$$\phi(L|N', L_*, \alpha, \beta) = N' \left[\left(\frac{L}{L_*} \right)^\alpha + \left(\frac{L}{L_*} \right)^\beta \right]^{-1}, \quad (8)$$

as it provides a good fit to the local luminosity function of IRAS-selected galaxies (Serjeant & Harrison 2005). The double power-law has 4 free parameters in total: the normalization factor, N' , the faint end slope, α , the bright end slope, β , and the characteristic luminosity, L_* , at which the transition from the two slopes occurs. For a given set of values of the free parameters, the probability that a source is observed with rest-frame luminosity L_i , and with an *effective* redshift $z_{\text{eff},i}$ (i.e. the redshift that the source would have at the distance d_i if peculiar motions were negligible) is thus given by

$$p_i = \frac{1}{N} \phi(L_i|N', L_*, \alpha, \beta) \frac{dV_c}{dz d\Omega}(z_{\text{eff},i}) \Omega \quad (9)$$

where dV_c is the comoving volume element and $L_{\text{min},i}$ is the minimum luminosity that can be observed at the distance and the redshift of the i -th source, given the flux limit of the sample, i.e.

$$L_{\text{min},i} = \frac{4\pi d_i^2 F_{\text{lim}}}{(1+z_i)k(z_i)}. \quad (10)$$

\tilde{N} is the total number of objects with $L \geq L_{\text{min},i}$ and $F \geq F_{\text{lim}}$ given the model LF

$$\tilde{N} = \Omega \int_{z_{\text{min}}}^{z_{\text{max}}} dz \frac{dV_c}{dz d\Omega}(z) \int_{L_{\text{min}}}^{\infty} d\log L \phi(L|N', L_*, \alpha, \beta), \quad (11)$$

where $L_{\text{min}} = \max[\log L_{\text{min},i}, \log L_{\text{lim}}(z)]$, and $L_{\text{lim}}(z)$ is the

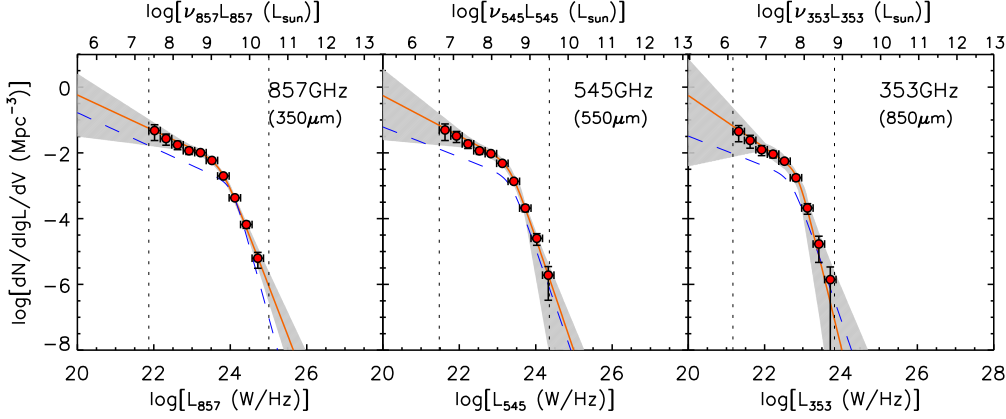


Figure 12. Local luminosity functions at 857 GHz (350 μm), 545 GHz (550 μm) and 353 GHz (850 μm) derived using the maximum likelihood parametric method (orange curve) compared with that measured via the $1/V_{\text{max}}$ method (red dots with error bars). The grey shaded regions correspond to the 68 per cent confidence interval for the parametric estimate. The predictions by Serjeant & Harrison (2005) are also shown for comparison (dashed curve). The meaning of the vertical dotted lines is the same as in Fig. 10.

Band (GHz)	Band (μm)	$\log[N'(\text{Mpc}^{-3})]$	$\log[L_*(\text{W/Hz})]$	α	β
857	350	$-2.28^{+0.16}_{-0.20}$	$23.76^{+0.13}_{-0.11}$	$0.54^{+0.13}_{-0.17}$	$3.03^{+0.33}_{-0.23}$
545	550	$-2.30^{+0.18}_{-0.50}$	$23.33^{+0.26}_{-0.12}$	$0.61^{+0.27}_{-0.17}$	$3.43^{+2.5}_{-0.31}$
353	850	$-2.54^{+0.38}_{-0.56}$	$22.88^{+0.25}_{-0.20}$	$0.80^{+0.38}_{-0.33}$	$4.76^{+2.40}_{-1.29}$

Table 6. Parameters of the maximum likelihood luminosity functions [eq. (8)] at 857 GHz (350 μm), 545 GHz (550 μm), 353 GHz (850 μm). At 217 GHz (1382 μm) the very limited statistic does not allow us to derive any meaningful constraint on the model parameters. The quoted errors correspond to the 68% confidence intervals.

luminosity corresponding to the flux density limit at redshift z , while z_{min} and z_{max} are the minimum and the maximum redshifts observed in the flux-/luminosity-limited sample. The probability defined by eq. (9) is independent of the normalization N' as the latter cancels out in the ratio between the differential and cumulative luminosity functions. This is what makes the maximum likelihood approach independent of local inhomogeneities under the assumption of a *universal* luminosity function. The probability of observing N objects with luminosities $\{L_1, L_2, \dots, L_N\}$, with redshifts $\{z_1, z_2, \dots, z_N\}$ and with physical distances $\{d_1, d_2, \dots, d_N\}$ is

$$P = \frac{\tilde{N}^N e^{-\tilde{N}}}{N!} \prod_{i=1}^N p_i \quad (12)$$

where we have assumed that the number of detected sources follows a Poisson distribution with expectation value equal to \tilde{N} defined by eq. (11). In order to account for the incompleteness in our samples we follow Patel et al. (2012), by replacing the total number of objects (N) with $\sum w_i$ and introducing a weighting term, $w_i/\langle w \rangle$ ($\langle w \rangle$ being the average weight) as an exponent of the individual source likelihoods, such that

$$P \propto \tilde{N}^{\sum w_i} e^{-\tilde{N}} \prod_{i=1}^N p_i^{w_i/\langle w \rangle}. \quad (13)$$

By maximizing the probability P (i.e. the likelihood of the sample) one obtains the set of values of N' , L_* , α and β that make the observed data set the “most probable” one. Following the same bootstrap resampling method used to

measure the luminosity function via the $1/V_{\text{max}}$ method, we have estimated the maximum likelihood values of the free parameters for each of the simulated samples. The derived luminosity functions and their uncertainties are shown in Fig. 12. They are fully consistent with those derived from the $1/V_{\text{max}}$ method. We have checked that the consistency with the $1/V_{\text{max}}$ results is maintained even if we use a power-law/Gaussian analytic model⁵ for the LF, like the one suggested by Saunders et al. (1990),

$$\phi(L|N', L_*, \alpha, \sigma) = N' \left(\frac{L}{L_*} \right) \exp \left[-\frac{1}{2\sigma^2} \log^2 \left(1 + \frac{L}{L_*} \right) \right]. \quad (14)$$

The agreement between the two estimates further supports the conclusion that inhomogeneities associated with large scale structure in the local Universe are not an issue in our analysis. Besides, overdensities associated with galaxy clusters in the local Universe are less pronounced in far-infrared/sub-mm surveys than in optical/near-infrared surveys. In fact such regions, especially their dense core, are dominated by ellipticals which have relatively low dust emission. The maximum likelihood values of the parameters and their 68% confidence intervals, derived from the distribution of values produced by the bootstrap, are given in Table 6 for the 3 higher frequencies (857, 545 and 353 GHz). As illustrated by Fig. 12 the luminosity range covered by the 217

⁵ In this model the LF behaves as a power law for $L \ll L_*$ and as a Gaussian in $\log L$ for $L \gg L_*$

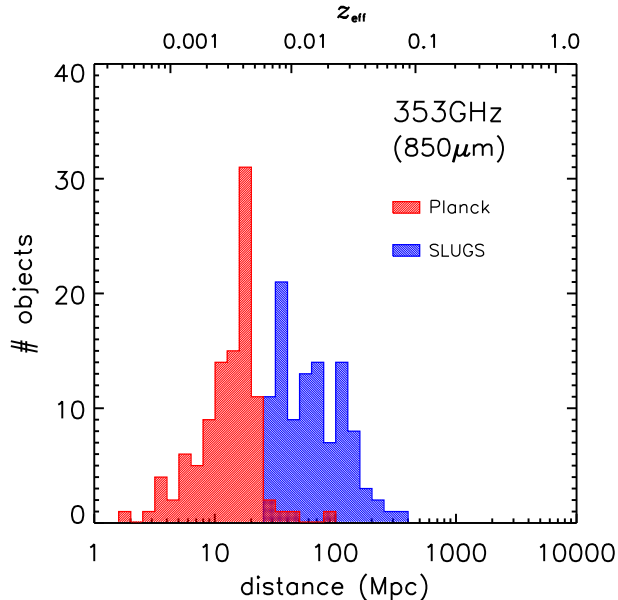


Figure 13. Distribution of source (physical) distances in the SLUGS sample (blue histogram) and in the *Planck* flux-limited sample used to measure the luminosity function (red histogram). The value of the redshift corresponding to a given distance (effective redshift, see text) is shown in the upper x-axis.

GHz sample is too small to allow a reliable estimate of the slopes α and β .

As a sanity check, we use eq. (6) of Planck Collaboration VII (2012) to derive the normalization of the Euclidean plateau of the number counts from the estimated luminosity function and compare it with the values quoted in § 2.3. The results, based on the best-fit parameters listed in Table 6, are 509, 109 and $14 \text{ Jy}^{1.5} \text{ sr}^{-1}$ at 857, 545 and 353 GHz, respectively, in excellent agreement with those derived from the observed number counts.

4 COMPARISON WITH EARLIER ESTIMATES

4.1 Comparison with Dunne et al. (2000) and Serjeant & Harrison (2005)

Dunne et al. (2000) have carried out a follow-up program at $850 \mu\text{m}$ with SCUBA – the SCUBA Local Universe Galaxy Survey (SLUGS hereafter) – of a sample of galaxies selected from the *IRAS* Bright Galaxy Sample (BGS; Soifer et al. 1989). The BGS is complete to a $60 \mu\text{m}$ flux limit of 5.24 Jy at $|b| > 30^\circ$ and $\delta > -30^\circ$. The SLUGS sample includes all BGS galaxies with declination in the range $-10^\circ < \delta < 50^\circ$ and with velocities above $v_{\min} = 1900 \text{ km s}^{-1}$ (corresponding to a minimum redshift $z_{\min} = v_{\min}/c = 0.0063$). The minimum velocity is chosen to exclude those galaxies whose angular size exceeds the SCUBA field-of-view (~ 2 arcminutes). In Fig. 13 we compare the distribution of source distances in the SLUGS sample with that of the *Planck* flux-/luminosity-limited sample from which the luminosity function has been measured. The peak observed around 17 Mpc is partially due to the Virgo cluster. However we have checked that the estimated luminosity functions do not

change significantly if the region associated with the Virgo Cluster is masked off.

The overlap between the *Planck* and the SLUGS samples is poor (only 5 galaxies are in common) mainly because of the low- z cut adopted by Dunne et al. (2000). The luminosity function derived by the latter authors is shown by the blue squares in Fig. 10. It agrees with the *Planck* measurements for $L_{353\text{GHz}} \gtrsim 10^{23} \text{ W/Hz}$ but lies significantly below them at fainter luminosities. A likely explanation of the difference is the bias against cold dusty galaxies implicit in the SLUGS sample. In fact, the selection at $60 \mu\text{m}$ combined with the imposed minimum redshift tends to favor galaxies with relatively bright infrared luminosities which usually have warmer SEDs (e.g. Smith et al. 2011). This bias has been demonstrated by Vlahakis et al. (2005) and, more recently, by Planck Collaboration XVI (2011) who have performed a detailed analysis of the SED properties of a sample of low-redshift galaxies extracted from the ERCSC. We confirm those results by comparing the sub-mm/far-infrared colours of the SLUGS sample with those of the *Planck* sources used to derive the luminosity function at $850 \mu\text{m}$. The results are shown in Fig. 14 together with the track of a grey-body with dust emissivity index $\beta = 1.3$ and temperatures ranging from 20 to 50 K (in steps of 5 K). The SLUGS sample has higher dust temperatures than the $850 \mu\text{m}$ *Planck*-selected sample, and the difference is more pronounced for galaxies with lower $850 \mu\text{m}$ luminosities (yellow dots).

Serjeant & Harrison (2005) have gone one step further and derived the local luminosity function of galaxies at many wavelengths from $70 \mu\text{m}$ to $850 \mu\text{m}$ by modeling the SEDs of all 15411 galaxies from the redshift survey of the IRAS Point Source Catalogue (PSCz; Saunders et al. 2000). The PSCz survey covers 84 per cent of the sky to a depth of 0.6 Jy at $60 \mu\text{m}$ and has a median redshift of 8400 km s^{-1} (i.e. $z = 0.028$). Starting from the *IRAS* measurements at 60 and $100 \mu\text{m}$, Serjeant & Harrison have exploited the strong correlation observed in the SLUGS between the far-infrared luminosity and the sub-mm/far-infrared colour to predict the sub-mm fluxes of each of the PSCz galaxies. As stated by the authors, these predictions are sufficient to define the sub-mm fluxes to within a factor of 2. The Serjeant & Harrison results at *Planck* wavelengths are shown by the dashed curves in Figs. 6 and 7 for the number counts and in Figs. 10 and 12 for the luminosity functions. Not surprisingly, since again we are dealing with an *IRAS*-selected sample, the agreement is good at high luminosities but *Planck*-based estimates are higher below the characteristic luminosity L_\star .

4.2 Comparison with Vlahakis et al. (2005)

To check whether the *IRAS* selection misses populations of sub-millimeter emitting galaxies Vlahakis et al. (2005) observed with SCUBA a sample of 81 galaxies selected from the Center for Astrophysics (CfA) optical redshift survey (Huchra et al. 1983). They found that the ratios of the mass of cold dust to the mass of warm dust for these galaxies is much higher than for the SLUGS galaxies, thus demonstrating that the SLUGS was missing a significant population of galaxies characterized by large proportions of cold dust. In

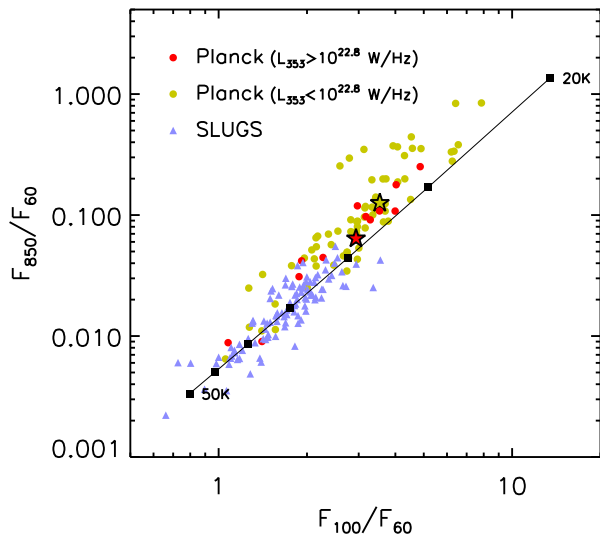


Figure 14. Sub-mm/far-infrared colour-colour plane for the 353 GHz (850 μ m) selected *Planck* sources with completeness above 80% and with luminosity $< 10^{22.8}$ W/Hz (red dots) or $> 10^{22.8}$ W/Hz (yellow dots). The stars represent the mean values. The SLUGS sample (Dunne et al. 2000; blue triangles) is shown for comparison. The solid line is the track for a grey-body with dust emissivity index $\beta = 1.3$ and temperatures ranging from 20 up to 50 K in steps of 0.5 K.

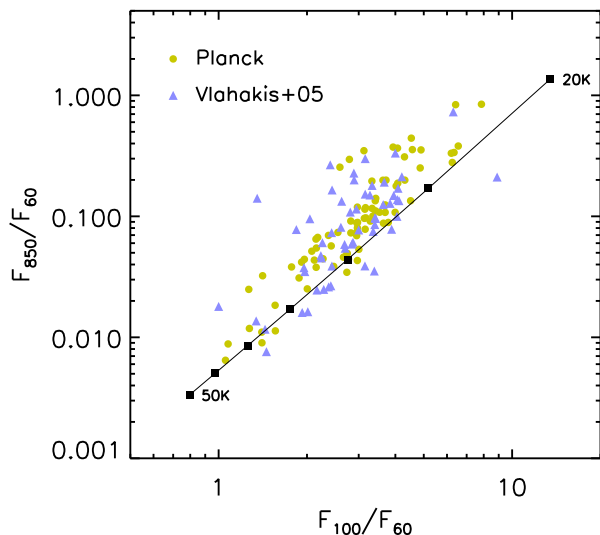


Figure 15. Sub-mm/far-infrared colour-colour plane for the 353 GHz (850 μ m) selected *Planck* sources with completeness above 80% (yellow dots) and for the sample of optically selected galaxies of Vlahakis et al. (2005; blue triangles). The solid line is the same as in Fig. 14.

fact, the 850 μ m luminosity function derived by Vlahakis et al. is higher than the one derived from the SLUGS.

The green dots in the 850 μ m panel of Fig. 10 show the luminosity function of Vlahakis et al. obtained with the method of Serjeant & Harrison, but using sub-mm/far-IR colour relations re-calibrated on the SLUGS and the op-

tically selected samples together⁶. The result is in better agreement with the ERCSC luminosity function, and, as expected, the sub-mm/far-infrared colours of the Vlahakis et al. sample are consistent with those of the 850 μ m *Planck*-selected sample, as shown in Fig. 15.

4.3 Comparison with Vaccari et al. (2010)

Vaccari et al. (2010) have estimated the local luminosity functions of galaxies selected at 250, 350 and 500 μ m in the Lockman Hole and XFLS fields (14.7 deg²) observed during the Herschel Science Demonstration Phase (SDP) of HerMES (the *Herschel* Multi-tiered Extragalactic Survey; Oliver et al. 2012). Their samples cover the redshift range $0 < z < 0.2$ and comprise 210 sources at 350 μ m and 45 sources at 500 μ m; at both wavelengths they have spectroscopic redshifts for $\simeq 85\%$ of their sources.

We have converted to 545 GHz (550 μ m) their 500 μ m luminosity function by assuming $\alpha = 2.7$, as this is the mean value of the sub-mm spectral index found from the analysis of the SED of local galaxies in the *Planck* sample (Clemens et al., in prep.). Their results, shown by the blue triangles in Fig. 10, generally agree, within the uncertainties, with ours, even though Vaccari et al. did not take into account any evolutionary correction, while significant evolution between $0 < z < 0.1$ and $0.1 < z < 0.2$ was reported, at 250 μ m, by Dye et al. (2010) and Dunne et al. (2011).

The estimates of the local (sub-)mm luminosity function presented here are the first derived from a complete all-sky (sub-)mm selected sample of galaxies. Together with the estimates of the luminosity functions of higher redshifts galaxies produced by *Herschel* (Eales et al. 2010b; Gruppi et al. 2010; Lapi et al. 2011), they will provide a critical constraint for any model of galaxy evolution.

5 CONCLUSIONS

The *Planck* ERCSC has provided the first samples of truly local (distance $\lesssim 100$ Mpc) galaxies blindly selected at (sub-)mm wavelengths, large enough to allow us to obtain accurate determinations of the local luminosity function at 857, 545 and 353 GHz down to luminosities one order of magnitude fainter than previous estimates and well below the characteristic luminosity L_* . We have also obtained the first estimate, albeit over a limited luminosity range, of the local luminosity function of dusty galaxies at 217 GHz. To get there several steps were necessary:

- Identification of the ERCSC flux density measurement most appropriate for our galaxies and application of suitable corrections,
- separation of dusty sources from radio loud AGNs,
- removal of Galactic sources,
- determination of the completeness limits at each frequency,

⁶ The 850 μ m luminosity function derived by Vlahakis et al. using the method of Serjeant & Harrison is in perfect agreement with that directly measured from the optically selected sample alone. We decided to show the former because it has a better statistic.

- correction of *Planck* fluxes for the contribution of *CO* lines.

Although spectroscopic redshifts are available for all galaxies in our samples, they may not be good distance indicators because of the potentially important contributions of peculiar motions. Therefore we have used, as far as possible, redshift-independent distance estimates that are available for most sources. The effect of local inhomogeneities in the galaxy distribution was investigated by means of the V/V_{\max} test in different luminosity bins. We also used, in addition to the classical $1/V_{\max}$ estimator, a parametric maximum likelihood estimator of the luminosity function, that is immune to the effect of inhomogeneities.

The derived luminosity functions are in good agreement, at high luminosities, with those obtained using follow-up observations of 60 μm selected IRAS galaxies (Serjeant & Harrison 2005; Dunne et al. 2000). Below the characteristic luminosity, L_* , however, our estimates are significantly higher, due to the bias against cold, generally low-luminosity galaxies, inherent in the SLUGS sample, and close to the estimate by Vlahakis et al. (2005) based on SCUBA follow-up of an optically selected sample. Our estimates are also consistent with those by Vaccari et al. (2010) based on data from the HerMES survey at 350 and 500 μm .

A detailed analysis of the astrophysical properties (such as star-formation rates, dust masses, dust temperatures, infrared luminosity function etc.) of the galaxies used here to derive the local sub-mm luminosity function will be presented in a forthcoming paper (Clemens et al. in prep.).

ACKNOWLEDGEMENTS

This work was supported by ASI/INAF agreement I/072/09/0 and by PRIN MIUR 2009. We thank the anonymous referee for useful comments. J.G.N. acknowledges financial support from Spanish CSIC for a JAE-DOC fellowship. L.T., J.G.N. and L.B. acknowledge partial financial support from the Spanish Ministerio de Ciencia e Innovación under project AYA2010-21766-C03-01. This research has made use of Aladin and of the NASA/IPAC Extragalactic Database (NED) which is operated by the Jet Propulsion Laboratory, California Institute of Technology, under contract with the National Aeronautics and Space Administration.

REFERENCES

- Avni Y. & Bahcall J. N., 1980, *ApJ*, 235, 694
 Beichman C. A., Neugebauer G., Habing H. J., Clegg P. E., Chester T. J., 1988, *IRAS Explanatory Supplement*
 Bonnarel F. et al., 2000, 143, 33
 Boselli A. et al., 2010, *PASP*, 122, 261
 Ciesla L. et al., 2012, *A&A*, in press (astro-ph/1204.4726)
 Clements D. L., Dunne L. & Eales S., 2010, *MNRAS*, 403, 274
 Daddi E. et al., 2010, *ApJL*, 714, 118
 Dale D. A., et al., 2012, *ApJ*, 745, 95
 Davies J. I., et al., 2012, *MNRAS*, 419, 3505
 Dunne L., et al., 2011, *MNRAS*, 417, 1510
 Dunne L., Eales S., Edmunds M., Ivison R., Alexander P., Clements D. L., 2000, *MNRAS*, 315, 115
 Dye S. et al., 2010, *A&A*, 518, 10
 Eales S. et al., 2010, *PASP*, 122, 499
 Eales S. et al. 2010, *A&A*, 518, L23
 Eddington A. S., 1913, *MNRAS*, 73, 359
 Efstathiou G., Ellis R. S., Peterson B. A., 1988, *MNRAS*, 232, 431
 Gehrels N., 1986, *ApJ*, 303, 336
 Genzel R. et al. 2010, *MNRAS*, 407, 2091
 Gruppioni C. et al., 2010, *A&A*, 518, 27
 Gruppioni C., Pozzi F., Zamorani, G., & Vignali C. 2011, *MNRAS*, 416, 70
 Healey S. E., Romani R. W., Taylor G. B., Sadler E. M., Ricci R., Murphy T., Ulvestad J. S., Winn J. N., 2007, *ApJS*, 171, 61
 Huchra J., Davis M., Latham D., Tonry J., 1983, *ApJS*, 52, 89
 Herranz D., et al., 2012, *A&A* submitted, arXiv:1204.3917
 Lapi A. et al., 2011, *ApJ*, 742, 24
 Leroy A. K. et al., 2009, *AJ*, 137, 4670
 Mao R.-Q., Schulz A., Henkel C., Mauersberger R., Muders D., Dinh-V-Trung, 2010, *ApJ*, 724, 1336
 Moshir M. et al., 1992, *Explanatory Supplement to the IRAS Faint Source Survey, Version 2*, JPL D-10015 8/92 JPL, Pasadena
 Negrello M. et al., 2004, *MNRAS*, 352, 493
 Negrello M. et al., 2005, *MNRAS*, 358, 869
 Oliver S. et al., 2012, arXiv:1203.2562
 Papadopoulos P. P., van der Werf P., Xilouris E. M., Isaak K. G., Gao Y., Muehle S., 2011, arXiv:1109.4176
 Patel H., Clements D. L., Vaccari M., Mortlock D. J., Rowan-Robinson M. & Perez-Fournon I., 2012, *MNRAS* in press (astro-ph/1205.5690)
 Pilbratt G. et al., 2010, *A&A*, 518, 1
 Planck Collaboration, 2011, *The Explanatory Supplement to the Planck Early Release Compact Source Catalogue (ESA)*
 Planck Collaboration I, 2011, *A&A*, 536, A1
 Planck Collaboration VII, 2011, *A&A*, 536, A7
 Planck Collaboration XIII, 2011, *A&A*, 536, A13
 Planck Collaboration XIV, 2011, *A&A*, 536, A14
 Planck Collaboration XVI, 2011, *A&A*, 536, A16
 Planck Collaboration VII, 2012, *A&A* submitted, arXiv:1207.4706
 Polletta M., et al., 2007, *ApJ*, 663, 81
 Sandage A., Tammann G. A., Yahil A., 1979, *ApJ*, 232, 352
 Saunders W., Rowan-Robinson M., Lawrence A., Efstathiou G., Kaiser N., Ellis R. S., Frenk C. S., 1990, *MNRAS*, 242, 318
 Saunders W. et al., 2000, *MNRAS*, 317, 55
 Sanders D. B., Mozzarella J. M., Kim D. C., Surace J. A. & Soifer B. T., *AJ*, 126, 1607
 Schlegel D. J., Finkbeiner D. P., Davis M., 1998, *ApJ*, 500, 525
 Schmidt M., 1968, *ApJ*, 151, 393
 Serjeant S. & Harrison D., 2005, *MNRAS*, 356, 192
 Smith D. J. B., et al., 2011, *MNRAS*, 416, 857
 Soifer B. T., Boehmer L., Neugebauer G. & Sanders D. B., 1989, *AJ*, 98, 766

- Solomon P. M., Downes D., Radford S. J. E., Barrett J. W.,
1997, ApJ, 478, 144
Vaccari M. et al., 2010, A&A, 518, 20
Vlahakis C., Loretta D. & Eales S., 2005, MNRAS, 364,
1253
Wang L. & Rowan-Robinson M., 2009, MNRAS, 398, 109
Wright E. L., et al., 2010, AJ, 140, 1868
Yahil A., Sandage A., Tammann G. A., 1980, ApJ, 242,
448
Yahil A., Strauss M. A., Davis M., Huchra J. P., 1991, ApJ,
372, 380
Yao L., Seaquist E. R., Kuno N., Dunne L., 2003, ApJ, 588,
771